A smartphone camera for the structure from motion reconstruction for measuring soil surface variations and soil loss due to erosion

A. Vinci, F. Todisco, R. Brigante, F. Mannocchi and F. Radicioni

ABSTRACT

The suitability of a smartphone camera for the structure from motion (SfM) reconstruction for monitoring variations in soil surface characteristics and soil loss originated by a low intensity erosive event was evaluated. Terrestrial laser scanning (TLS) was used to validate the SfM model. Two surveys of the soil surface, one before and one after the rainfall event, were carried out for SfM and TLS. The point clouds obtained by the SfM were compared to the TLS point clouds (used as reference). From the point clouds, digital elevation models (DEMs) (0.01 m × 0.01 m) were obtained. The differences of the DEMs (DoDs) obtained from the two surveys for SfM and TLS were compared. To assess the uncertainty of the DEMs, from the DoDs the minimum level of detection was derived. The soil loss was evaluated from DoDs (for SfM and TLS, respectively) considering negative values as erosion and positive values as deposition. The SfM appears appropriate and sensitive for detecting small soil surface variations induced by low erosive events. The SfM estimated correctly the measured soil loss, while TLS underestimated 26%. Further studies could be carried out to consolidate these first results.

Key words | DEM, high resolution topography, interrill erosion, SfM photogrammetry, soil loss, TLS

A. Vinci (corresponding author)
F. Todisco
F. Mannocchi
Department of Agricultural, Food and Environmental Sciences,
University of Perugia,
Borgo XX Giugno 74,
06121 Perugia,
Italy
E-mail: *alessandra.vinci@unipg.it*

R. Brigante
F. Radicioni
Department of Engineering,
University of Perugia,
Via G. Duranti 93,
06125 Perugia,
Italy

INTRODUCTION

Soil erosion is defined as a displacement of solid particles originating from soil, rock, and other sediments. Soil is a key component of the 'Earth system' in controlling the biological, geochemical hydrological, and erosional cycles and also providing goods, resources, and services (Keesstra *et al.* 2012, 2016; Brevik *et al.* 2015). Soil is naturally removed by the action of water or wind, and by downward or downslope movement in response to gravity. Soil erosion is a key process of soil and land degradation. High and non-sustainable erosion rates are due to the human mismanagement of soils and can be due to many factors (Cerdà *et al.* 2016). For example, as assessed by Navarro-Hevia *et al.* (2016) and Cao *et al.* (2015), the soil erosion and erosion rates are more severe in proximity of roads, paved or not, and railways. Soil erosion is high in many types of cultivated land such as persimmon plantations (Cerdà *et al.* 2016) and vineyards (Tarolli *et al.* 2015; Rodrigo Comino *et al.* 2016; Prosdocimi *et al.* 2017). In these cases, the agricultural practices modify the soil characteristics and enhance land erosion vulnerability. Thus, erosion is considered to be one of today's most widespread environmental problems (Filin *et al.* 2013). Soil erosion affects micro-topography, leading to clogging of surface drainage systems, flooding, and destruction of the upper part of the soil structure cross section (Agassi & Bradford 1999). Soil micro-topography or surface roughness is used to describe soil surface variations at scales from a few millimeters to as much as 1 meter. In fact, soil micro-topography was used by Gómez & Nearing (2005) to control various hydrological processes such as depressional storage and time to runoff, by Thompson *et al.*

doi: 10.2166/nh.2017.075

(2010) to evaluate infiltration and runoff amount, and by Helming *et al.* (1998) to assess concentrated flow and occasional soil loss.

To detect soil erosion, laser scanners have proven their usefulness in many experiments (Eltner *et al.* 2013; Eltner & Baumgart 2015; Tarolli *et al.* 2015; Vinci *et al.* 2015, 2016). Recently, some studies have shown the suitability of the structure from motion (SfM) photogrammetry also. In fact, the SfM photogrammetry reveals superiority compared to two-dimensional (2D) and three-dimensional (3D) methods to detect gully erosion (Castillo *et al.* 2012; Kaiser *et al.* 2014; Frankl *et al.* 2015). Therefore, SfM was applied by Eltner *et al.* (2015) to rill erosion, and Smith & Vericat (2015), Vericat *et al.* (2014), Ouédrago *et al.* (2014), and Snapir *et al.* (2014) have used SfM to quantify soil erosion and roughness at bigger scales than applied here. Aucelli *et al.* (2016) applied digital photogrammetric analysis to evaluate the time and space evolution of erosion processes at catchment scale. At plot scale, Pérez-Cabello *et al.* (2012) quantified the post-fire changes of ground cover due to soil erosion processes using high spatial resolution photography. The performance of the SfM photogrammetry to assess soil erosion was tested at plot scale, at small and large catchments (Pérez-Cabello *et al.* 2012; Smith & Vericat 2015; Aucelli *et al.* 2016). SfM photogrammetry is scale dependent; at plot and hillslope scale, 3D reconstruction is a very efficient method for soil erosion studies, even outperforming terrestrial laser scanning (TLS) (Eltner *et al.* 2016). While the main advantage of laser scanning technologies is their ability to generate accurate and high-resolution point clouds scaled to a metric coordinate system with minimum software support, the high cost of acquiring hardware limits their widespread use (Nouwakpo *et al.* 2014). SfM photogrammetry offers the advantage of having considerably lower hardware acquisition costs than laser scanner systems. The main limitation of SfM photogrammetry, however, has been its reliance on survey instruments to accurately measure control points, and it still requires expensive equipment and trained users to process data and to reconstruct soil surfaces. However, advances in image feature detection, matching techniques and multi-view stereo (MVS) have led to the development of SfM photogrammetry (Ullman 1979), which can reconstruct 3D features using few control points (needed to transform a model to a given metric coordinate system). As stressed by Nouwakpo *et al.* (2014), the SfM method is suitable for generating interpolated digital elevation models (DEMs) at millimeter resolution, but in applications that would be detrimentally impacted by point cloud deformation (for example, soil erosion assessment), care must be taken to ensure fidelity between the modeled and real-life surfaces. Furthermore, one of the key advantages of modern SfM technologies over traditional photogrammetric software is the ability to process oblique imagery for dense 3D reconstruction. In fact for plot-scale applications, near-vertical photographs usually require specific platforms such as the rail mechanism used by Nouwakpo *et al.* (2014), while modern SfM technologies allow the camera to be handheld. Smith & Vericat (2015) tested 'oblique survey' at different scales, assessing that it can be used to generate high-resolution topography data at plot or hillslope scale. Also, Eltner *et al.* (2015) stressed the advantage of SfM photogrammetry for the assessment of plot-based soil erosion analysis. SfM photogrammetry can be performed using a consumer-grade digital camera, and therefore it is very flexible in its implementation by highly automated data processing. Smartphones now include high-resolution digital cameras and seem to be suitable for geodetic surveys (Micheletti *et al.* 2015a, 2015b; Prosdocimi *et al.* 2015); thus, for this paper, an Apple iPhone 6 Plus camera was used for the SfM photogrammetry.

The aim of this paper is to assess the capability of an Apple iPhone 6 Plus camera for SfM photogrammetry to detect soil surface elevation changes due to a rainfall event and to quantify soil erosion.

MATERIALS AND METHODS

Study site

The Masse experimental station for soil erosion measurements at the plot spatial scale has recently been set up by the Agricultural and Forest Hydraulics Research Division of the University of Perugia's Department of Agricultural, Food and Environmental Sciences. The station is located 20 km south of Perugia in the Umbria region (central Italy). The area is characterized by a hilly topography, where a specific analysis and precise quantification of erosion processes is particularly

important for establishing soil conservation measures. The station includes ten plots: four plots 8×22 m; two plots 4×22 m; two plots 4×11 m; and two plots 2×11 m. All plots are oriented according to the maximum slope (16%) and maintained as cultivated fallow. The soil is a Calcaric Cambisol (FAO 1998). Rainfall data are measured within the experimental station at 5-min time intervals. The hydraulic boundary of the plots was made from galvanized sheet, molded in order to give greater rigidity, and inserted into the ground to a depth of approximately 0.25 m; the sheet was also fastened to metal stakes placed at a distance of approximately 1 m. The lower side of each plot is delimited by a groove in the galvanized sheet with a rectangular section and variable height. The groove intercepts the runoff and conveys it to the storage tanks.

Total runoff and soil loss are measured after each erosive event (i.e., an event producing measurable runoff), applying the procedure described in Todisco *et al.* (2012). For the erosive event analyzed in the paper, the soil loss value measured in the surveyed plot was 3.32 $Mg \cdot ha^{-1}$.

All considered plots were maintained as cultivated fallow and rills were obliterated at the end of each erosive event (Todisco *et al.* 2012; Vinci *et al.* 2015).

Experimental set-up

The experiment was conducted on the 2×11 m plot size affected by a medium intensity rainfall event (9 November 2014) that produced interrill erosion. The total rainfall depth was 75 mm and the mean intensity was 1.23 $mm \cdot h^{-1}$. Two surveys of the plot surface microtopography were made: the first on 21 October 2014, when the soil surface was prepared to maintain the cultivated fallow, and the second on 11 November 2014, after the occurrence of the erosive event. No soil movement or leveling was made in the period between the surveys. Both surveys were carried out using a smartphone camera for the SfM photogrammetry and TLS for validation.

SfM image acquisition

An Apple iPhone 6 Plus (4.15 mm focal length, 8 Mpixel with pixel of 1.5 μ, aperture of f2.2) was used in this campaign. Two surveys were carried out, one before (hereafter referred to as the first survey) and one after (hereafter referred to as the second survey) the rainfall erosive event. Two 1080p60 HD videos of the entire plot (i.e., $1{,}920 \times 1{,}080$ pixels at 60 frames per second) were recorded, vertically from a height of approximately 2 m, walking all around the perimeter of the plot. To prevent variation of the focal length during video acquisition, the auto-focus ability of the camera was switched off and the lens taped at infinity focus. To lock exposure and focus on the Apple iPhone 6 Plus, a touch and hold on the focal point of the camera app until the auto exposure and auto focus (AE/AF) lock banner appeared on the screen was made. To improve the performance of the iPhone's native camera, some apps are available in the Apple Store. In particular, in this paper, in order to obtain the infinity focus, the digital single-lens reflex (DLSR) camera app was used. This app allows choosing the manual focus to enhance the subject of the photo and video, using the 'macro focus', to capture the smallest details, and the 'infinite focus' to define perfectly distant subjects. From the videos, 2,800 frames (at the same resolution as the native video, $1{,}920 \times 1{,}080$ pixel – full high definition (FHD)) were automatically extracted using a specifically created Matlab code. Although this procedure is not common, its main advantage over the direct acquisition of the photographs is the possibility of selecting a posteriori (after the survey) the best frames to avoid missing data on the SfM point cloud.

In order to ensure proper exterior orientation of the camera, 13 target ground control points (GCPs) were positioned along the fixed border of the plot and of the surrounding plots (Figure 1(b)). The GCPs were not placed directly on the soil surface, so as to ensure their stability during the event (the runoff could move and change their position) and their use for successive events (tillage operations after each erosive event could cause their damage or loss). The three-dimensional coordinates (X, Y, and Z) of the GCPs were collected by conventional terrestrial surveying from a Leica TS06 total station (which has a measurement accuracy of 2″ – 0.6 mgon – for angle measurement and 0.002 m + 2.0 ppm for range measurement).

Validation dataset

The validation dataset was based on the TLS geodetic survey. A Riegl LMS Z 420i was used to provide high

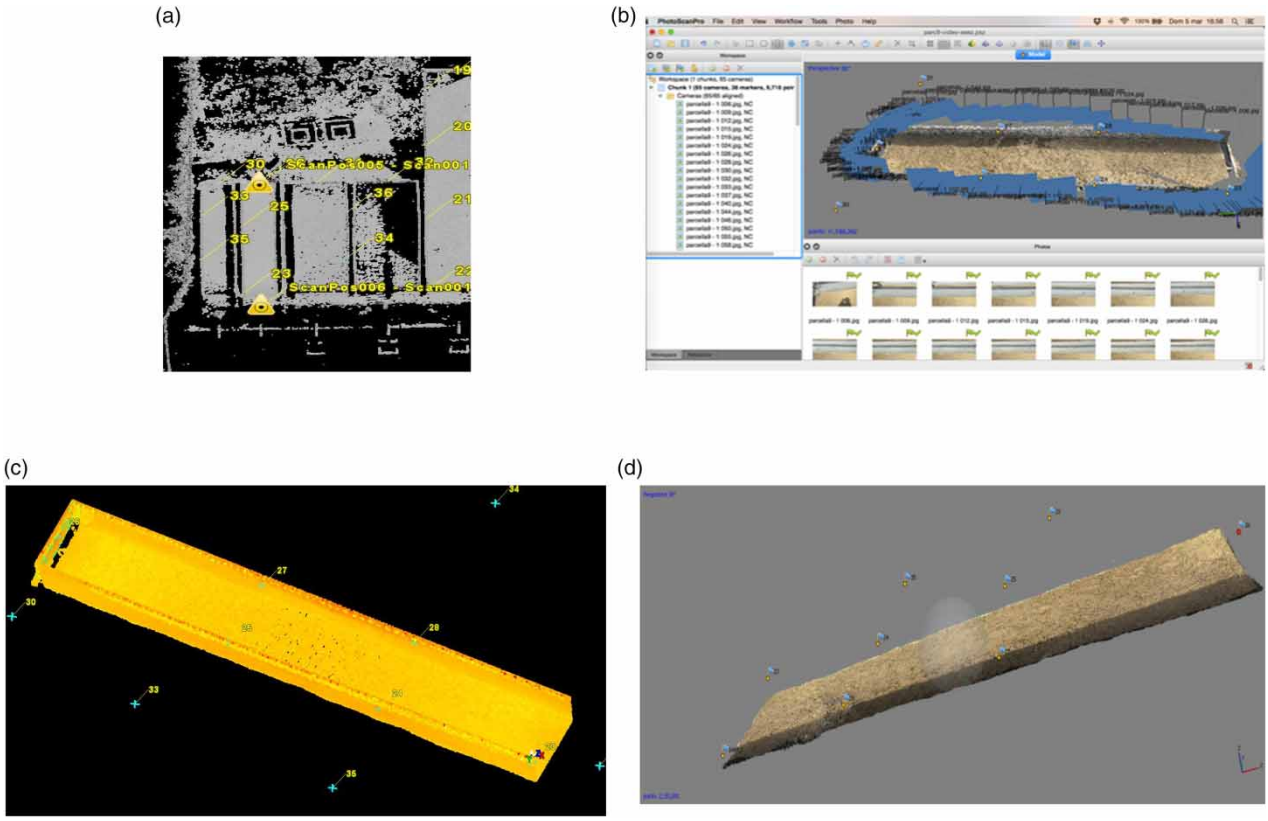

Figure 1 | Positions of the TLS scans (represented by the triangle) and positions of 13 targets (GCPs) (a); scheme of alignment frames (b); model of the 2 × 11 m plot obtained from the TLS survey (c); and dense point cloud model of the 2 × 11 m plot obtained from the SfM survey (d).

resolution geodetics data for the two surveys. Angular measurement resolution is 0.0025° in horizontal scan, 0.002° in vertical scan. The beam divergence of the scanner system is 0.25 mrad and the repeatability is 0.008 m.

For each TLS survey two scans were done with a scanning resolution of 0.01 m at 10 m (maximum distance between TLS and the soil). The positions of the instrument are shown as triangles in Figure 1(a). A single point cloud was obtained from each scan, the coordinates of which are given in a three-dimensional reference system. Each single scan must be aligned in a single cloud so another measurement was carried out using retro-reflective targets detected automatically by the TLS. The 3D coordinates of the targets were obtained by the Leica TS06 total station. The point clouds obtained, about 700,000 points for both the surveys, allowed the overall representation in an almost continuous survey area (Figure 1(c)). The errors derived from the TLS survey were co-registration errors (hereafter registration errors) and point cloud georeferencing errors (hereafter georeferencing errors). The registration errors were caused by the alignment between two scans in the TLS reference system. The georeferencing errors were caused by the transformation of the point clouds from the TLS coordinate system to the external (geodetic) coordinate system using the targets with known coordinate in the external system. A target-based registration was made, i.e., using the targets with known 3D coordinates placed in the overlap between the two point clouds. From this estimation process the registration errors were derived. The Leica Cyclone 3D Point Cloud Processing Software, using its internal least fit algorithm, quantified the registration errors and the georeferencing errors during the process of transformation. In order to optimize the results of the generated DEM, the scans were taken under cloud cover to reduce shadows and extreme contrasts with uniform illumination in the scans.

Post-processing

Photogrammetric processing and generation of point cloud

The frames extracted from the videos were used to create the SfM point clouds. Due to computational problems during the construction of the point cloud model, 100 frames were selected. The selection criterion was to have frames surveying the entire surface of the plot (a scheme of the image configuration with respect to the plot is shown in Figure 1(b)). Hence the photogrammetric processing and generation of 3D spatial data were performed using Agisoft PhotoScan (Full SfM-MVS commercial package). First, a calibration procedure was applied to calculate the calibration camera parameters using Agisoft Lens. Agisoft Lens is a freely available software package that utilizes planar grids to calculate the Brown–Conrady coefficients. The calibration grid was displayed upon a 30″ flat panel LCD screen. Imagery of the calibration grid was captured by the Apple iPhone 6 Plus at multiple angles. For each angle, multiple images were collected (using a tripod) and averaged in order to maximize noise reduction. The obtained calibration camera parameters (Table 1) were imported to Agisoft PhotoScan before the processing. PhotoScan was used to find matching points between overlapping images, to estimate the camera position (Figure 1(b)) and to build the sparse and dense point cloud model (Figure 1(d)). The settings used to obtain the dense point cloud are reported in Table 2.

As suggested by Micheletti *et al.* (2015b), to reduce co-registration errors of the SfM, the iterative closest points (ICP) algorithm has to be applied to the two datasets (in this case the first and the second survey). The ICP procedure described by Micheletti *et al.* (2015a) was applied.

The point cloud model was then imported into QGis software (version 2.2) to create the grid digital elevation model (DEM) 0.01 m × 0.01 m.

Table 1 | Parameter camera calibration obtained by Agisoft Lens

Parameter camera calibration		
Focal length (pixel)	**Principal points coordinates (pixel)**	**Radial distortion coefficients (Brown 1966) (pixel)**
$f_{x,pix}$ 2.9897×10^3	$c_{x,pix}$ 1.5977×10^3	k_1 6.9486×10^{-2}
		k_2 -1.6000×10^{-1}
		k_3 -3.7224×10^{-2}
$f_{y,pix}$ 2.9903×10^3	$c_{y,pix}$ 1.2166×10^3	p_1 -4.4554×10^{-4}
		p_2 -9.1972×10^{-5}

Table 2 | Parameters used for the dense point cloud reconstruction from Apple iPhone 6 Plus survey

Settings Agisoft PhotoScan		
Parameters for the align photos	**Parameters for build dense cloud**	**Parameters build mesh**
Accuracy: high	Quality: ultra high	Surface type: height field
Pair selection: disabled	Depth filtering: aggressive	Source data: sparse cloud
Key point limit: 100,000		Face count: high (1,550,692)
Tie point limit: 1,000		Interpolation: enabled
		Point classes: all

TLS processing and generation of DEM

The point cloud obtained by the TLS for each survey was used to create a discrete square mesh DEM model with a resolution of 0.01 m on the ground and a precision of approximately 0.01 m (evaluated using ten check points) in all dimensions. Leica Cyclone software was used for this purpose.

Validation of SfM point clouds and DEMs

Quantitative validation of SfM-derived topographic data against those derived from more conventional methods (in this case TLS) is prerequisite to confident application to a real-world problem (Smith *et al.* 2015). Thus, to evaluate the performance of the Apple iPhone 6 Plus camera for reconstructing the plot surface and detecting the elevation variations, two different analyses were made. To check for any plot scale surface deformation in SfM surface reconstruction (Nouwakpo *et al.* 2014), a cloud-to-cloud closest point cloud distance (C2C) analysis between the point clouds obtained by the camera and by the TLS surveys was made. The second comparison

was carried out using the DoDs derived by SfM and TLS. The C2C and DoD methods (also called point-to-point and raster-to-raster) give smaller errors than other methods such as point-to-raster (Smith *et al.* 2015; Smith & Vericat 2015).

The C2C comparison was made using the free software Cloud Compare V2. The SfM and TLS point clouds were aligned using a point-picking method followed by a fine registration operation based on the iterative closest point (ICP) method. The C2C method computes for each point of a reference point cloud (here TLS point cloud), the distance to the closest point in the compared point cloud (here SfM point cloud).

To validate the SfM dataset, the difference of the DEM ($DoD_{TLS\text{-}SfM}$) was obtained by the subtraction of the TLS-DEM from the SfM-DEM for both surveys. Therefore, the comparison was made using two independent DoDs, i.e., differencing SfM-TLS first survey DEMs ($DoD_{TLS\text{-}SfM,\ 1}$) and differencing SfM-TLS second survey DEMs ($DoD_{TLS\text{-}SfM,\ 2}$). The differences between SfM-derived topographic data and the TLS validation dataset were investigated using mean absolute error (MAE), root mean square error (RMSE), and standard deviation of error (SDE).

Evaluation of the soil loss mapping and quantification

The DEM of the difference (DoD) for SfM and TLS was derived by the subtraction of the old DEM (first survey) from the new DEM (second survey). Thus, the differences between TLS first and second survey DEMs (DoD_{TLS}) and the differences between SfM first and second survey DEMs (DoD_{SfM}) were obtained.

The DoD approach, gridded representations of the surface elevation, is differenced to quantify microtopographic changes (e.g., Nouwakpo & Huang 2012). This method is fast, but can result in detrimental loss of spatial information on complex surfaces and is susceptible to uncertainties due to the interpolation process from point cloud to gridded data structure (Nouwakpo *et al.* 2014). On the derived DoDs, negative values in the cells indicate erosion (surface lowering), positive values deposition, and a very low or zero value no change (e.g., Martínez-Casasnovas *et al.* 2002; Vericat *et al.* 2014; Smith & Vericat 2015). The significance of these changes will be controlled by the errors and by topographic uncertainties in each DEM. Following the approach described by Wheaton *et al.* (2010), an uncertainty analysis to define the minimum threshold of detection to recognize the real elevation changes from errors/uncertainties was made. The threshold, defined as minimum level of detection (i.e., $_{min}$LoD), was estimated using a probabilistic approach. In particular, as defined by Smith & Vericat (2015), the critical threshold error is equal to:

$$_{\min}LOD = t\sqrt{SDE_{new}^2 - SDE_{old}^2} \tag{1}$$

where t is the Student's critical value at a chosen confidence interval and SDE is the SDE of the DEMs (in this case first and second survey). The Student's t-value can be calculated by:

$$t = \frac{\left|z_{DEM_{new}} - z_{DEM_{old}}\right|}{\delta_{DOD}} \tag{2}$$

with numerator the absolute value of DoD and δ_{DOD} the error of the DoD. Using the 90% confidence interval, $t = 1.65$. The analysis was applied to the DoD obtained for the TLS and SfM (i.e., DoD_{TLS} and DoD_{SfM}).

The mapping and quantification of the sediments produced by the rainfall event that occurred on 9 November 2014 was based on the DoD obtained using the SfM (DoD_{SfM}) and the TLS (DoD_{TLS}) considering only the values above the $_{min}$LoD.

The sediment production rate per unit area was calculated according to the equation proposed by Martínez-Casasnovas (2000):

$$SPR = \frac{(ED \cdot GR^2 \cdot B_d)}{A} \tag{3}$$

where SPR is sediment produced by the rainfall event ($Mg{\cdot}ha^{-1}$), ED is sum of the elevation differences (m), GR is grid resolution (m), B_d is bulk density of the soil top layer ($Mg{\cdot}m^{-3}$), and A is area of the plot (ha).

To estimate the bulk density, during the surveys ten samples of soil were taken and analyzed. An average value of 1.26 $Mg{\cdot}m^{-3}$ was measured and used in Equation (3) as the bulk density of the soil top layer.

RESULTS

Assessing errors of SfM and TLS

The TLS scans were merged to create the full topographic model at plot scale using a target-based registration as explained above. Average registration error (MAE of targets) was about 0.0058 m and the georeferencing error (RMSE of GCPs) was about 0.0032 m for the two surveys (Table 3). Both TLS point clouds result in an average point density of about 30,000 points per m^2.

For the SfM surveys 13 GCPs were used. The RMSE of the control points, derived by the Agisoft PhotoScan, was 0.0064 m for the first survey and 0.0053 m for the second survey. The ICP procedure, applied between the two surveys, ensures a better coordinate system alignment, so the georeferencing error decreases. After the ICP procedure, the georeferencing error of the first survey was equal to 0.0043 m. Therefore, as suggested by Smith & Vericat (2015), a comparison of topographic models to check for any misalignment against the TLS datasets was made. No systematic georeferencing error was observed (with a 0.01 m grid size).

SfM validation based on TLS dataset

The results of the C2C comparison between the SfM point cloud and the TLS point cloud are reported in Table 4 and in Figure 2(a) (first survey) and Figure 2(c) (second survey). The elevation values of the point clouds reported in Figure 2(a) and 2(c) were derived by the difference between the reference cloud (TLS) and the compared cloud (SfM). In Figure 2(b) and 2(d), the distribution of the errors derived from the comparison is reported. For the first survey the difference values between SfM and TLS were lower than the difference values obtained for the second survey. In fact, for the first survey the MAE was 0.015 m, the SDE 0.01 m, and the RMSE 0.018 m while the MAE was 0.009 m, the SDE 0.008 m, and the RMSE 0.011 m for the second survey. The distribution of the errors derived from the C2C first survey (Figure 2(b)) shows symmetry in correspondence of the value −0.016 m and the maximum positive value is 0.006 m. Therefore, several areas of the SfM point cloud results were lower than the TLS point cloud for the first survey. For the second survey, the C2C comparison showed a good agreement, both MAE and SDE are sub-centimeter and the distribution of the errors (Figure 2(d)) were symmetrical in correspondence of the 0 value (i.e. the higher frequency obtained by the comparison is equal to 0).

Table 3 | Summary of registration (i.e., MAE of target) and georeferencing errors (i.e., RMSE on GCPs) derived from TLS and SfM surveys

Survey	Registration error (m)	Georeferencing error (m)
TLS-first survey	0.0058	0.0032
TLS- second survey	0.0058	0.0030
SfM-first survey		0.0043
SfM-second survey		0.0032

Table 4 | Summary of the errors in the validation of SfM surveys with TLS surveys

Method	Survey	Validation points	MAE (m)	SDE (m)	RMSE (m)
C2C comparison	First survey	1,104,137	0.015	0.01	0.018
	Second survey	7,528,769	0.009	0.008	0.011
DoD comparison (0.01 × 0.01 m grid)	First survey	46,284	0.012	0.006	0.015
	Second survey	46,980	0.001	0.007	0.005

Differences between the two SfM-based DEMs and TLS-based DEMs are summarized in Table 4. The comparison confirmed the major differences for the first survey with a MAE equal to 0.012 m, with a variability of SDE equal to 0.006 m, and a RMSE equal to 0.015 m. The analysis seems to show that $DEM_{SfM,1}$ had lower results everywhere than the $DEM_{TLS,1}$ (in fact, the range of the differences is −0.028 to −0.002 on the $DEM_{TLS\text{-}SfM,\ 1}$). In common with the C2C comparison, the distribution of the errors (Figure 3(c)) resulted as nearly normal and the mean of the errors is −0.016 m. In general, also for the second survey, the comparison between the DEMs confirmed the results obtained from the C2C analysis. The values obtained (especially the MAE and the RMSE, Table 4) were lower than those obtained by the C2C comparison. In fact $MAE_{DoD,2} = 0.001$ m versus $MAE_{C2C,2} = 0.009$ m and $RMSE_{DoD,2} = 0.005$ m versus $RMSE_{C2C,2} = 0.011$ m, while the variability was nearly the same with $SDE_{DoD,2} = 0.007$ m and $SDE_{C2C,2} = 0.008$ m.

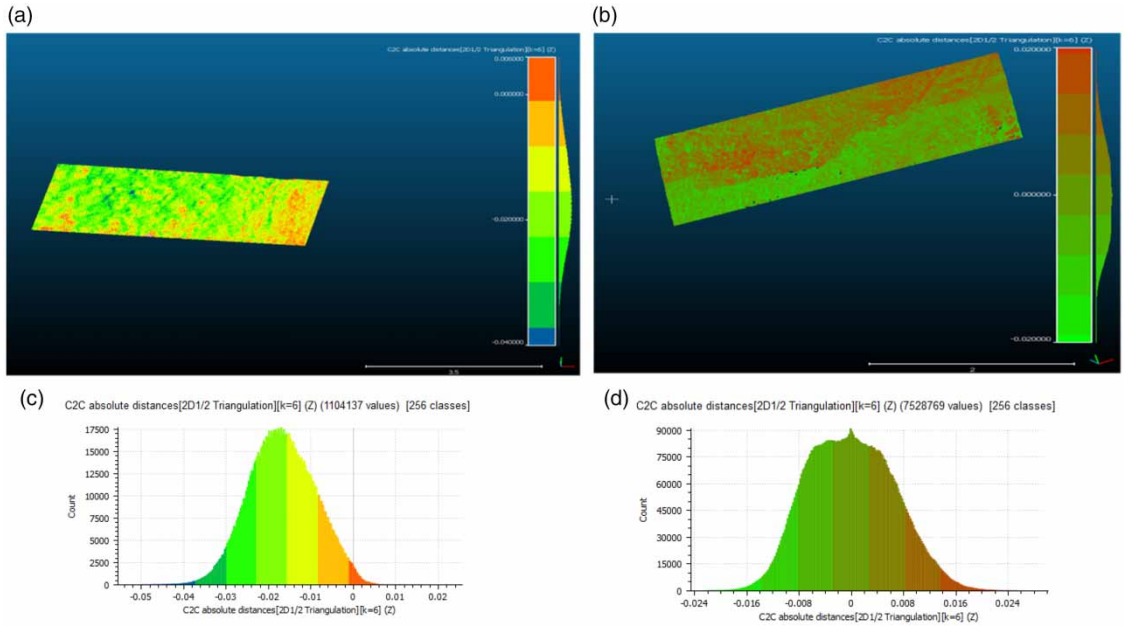

Figure 2 | Point cloud derived from the C2C comparison for the first survey (a) with relative distribution of the values (b) and for the second survey (c) with the relative distribution (d).

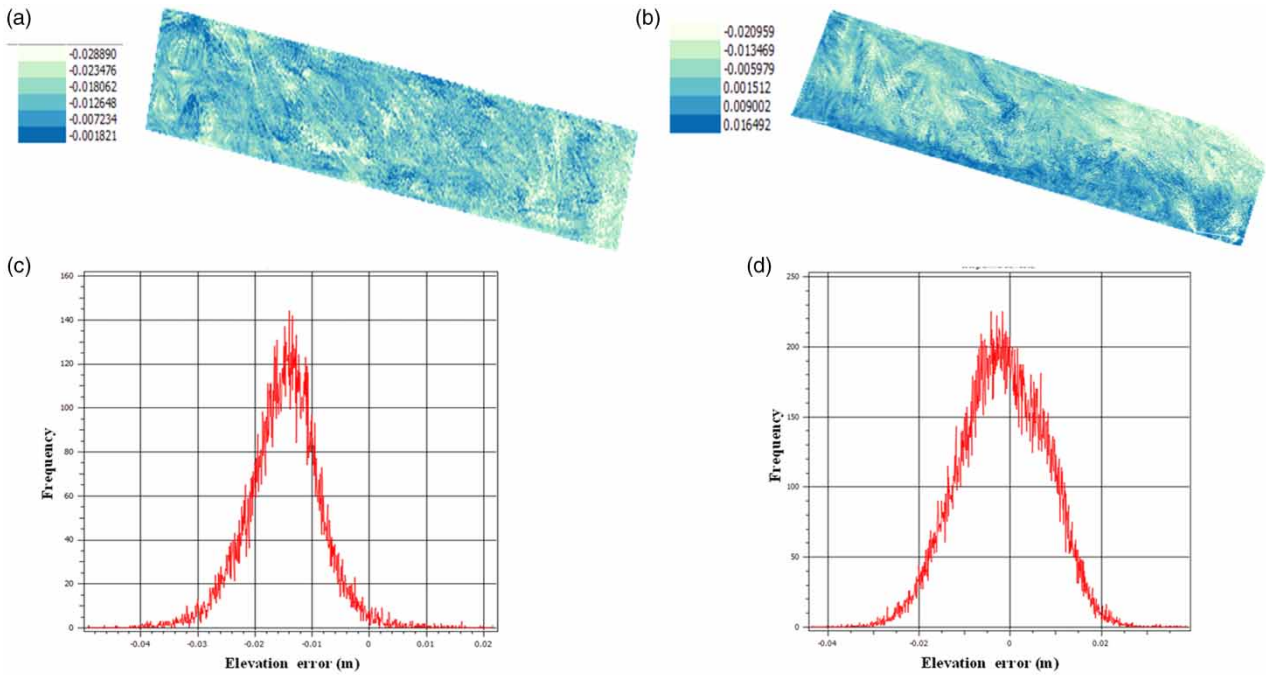

Figure 3 | DEM of the differences (DoD) for the first survey (a) and the second survey (b); distribution of the elevation errors (m) for the first (c) and the second (d) survey.

In Figure 4(a) and 4(d), DoD_{SfM} and DoD_{TLS}, obtained by the subtraction of the grids [$DEM_{new} - DEM_{old}$] are reported. The DoD_{SfM} (Figure 4(a)) shows a general lowering with a maximum value of −0.0353 m and a minimum of −0.0008 m, while the DoD_{TLS} (Figure 4(d)) shows a maximum lowering of −0.024 m and a maximum rising of 0.004 m.

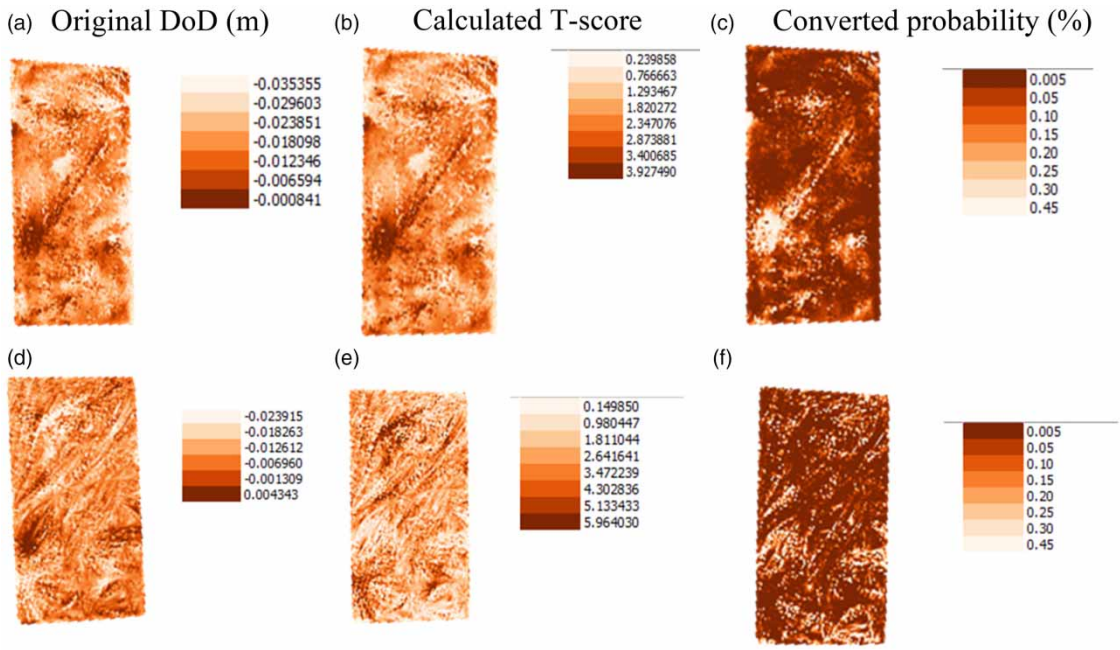

Figure 4 | DEM of the differences (DoD) for SfM (a), t-score obtained from Equation (2) (b), cumulative distribution probability (c); DEM of the differences (DoD) for TLS (d), t-score obtained from Equation (2) (e), cumulative distribution probability (f).

In Figure 4(b) and 4(e), the t-score maps for SfM and TLS, respectively, calculated by Equation (2), are reported. In correspondence of the lowest values of the DoD (absolute value, i.e., in the DoDs' deeper areas) the lowest result is for t-values, i.e., near to zero (soft areas).

The probability maps associated with t-values for SfM (Figure 4(c)) and TLS (Figure 4(f)) are reported. The light areas have high values, i.e., a high probability of non-exceedance, therefore representing the uncertainty areas (and not considered for the assessment of erosion/deposition). The deep areas correspond to a low probability of non-exceedance (high t-values) thus represent a lowering/raising significantly at 90% confidence interval.

Soil loss

The DoDs derived from the SfM photogrammetry survey (Figure 4(a), DoD_{SfM}) and from the TLS survey (Figure 4(d), DoD_{TLS}) are reported. As described above, these DEMs clearly show the areas where erosion occurred (negative difference values) and the areas where deposition occurred (positive difference values, visible only on the DoD_{TLS}).

Net erosion is evaluated as the difference between the sum of erosion pixels and the sum of deposition pixels, considering the pixels above the $_{min}$LoD.

For the SfM, the sum of the deposition pixels were equal to 0, so the net erosion equal to the sum of the erosion pixels was equal to 3.25 Mg·ha^{-1} in the plot. For the TLS, the sum of the erosion pixels was 7.06 Mg·ha^{-1} and the sum of the deposition pixels equal to 4.59 Mg·ha^{-1}, with a net erosion of 2.47 Mg·ha^{-1}. The two methods seem to give good results, but TLS underestimates the measured soil loss, 3.32 Mg·ha^{-1}. The best estimate was obtained using SfM, according to which the soil loss was nearly the measured value. The underestimation of the TLS can be due to noise on the first survey. Furthermore, the type of TLS used in this paper seems to be more suitable for other applications.

DISCUSSION

In this paper a plot of 2 m × 11 m was surveyed using a smartphone camera for the SfM reconstruction. The capability of the SfM to detect topographic changes and sediment budgets at the plot scale has also been assessed

by other authors (e.g., Nouwakpo *et al.* 2014; Micheletti *et al.* 2015b; Smith & Vericat 2015). The changes of the soil surface are not only due to soil water erosion, as there are also consolidation processes and changes in the soil surface due to the chemical composition of the soils. For example, Zhao *et al.* (2015) showed that a relationship exists between soil quality indicators and topography (slope and elevation); Martín-Moreno *et al.* (2016) showed that sediment yield and erosion depend on three main factors, i.e., slope, use of the surface cover, and plant establishment; Ochoa *et al.* (2016) showed that the soil erosion risk is highly influenced by the climatic seasonality and topographical conditions.

Previous studies (e.g., Micheletti *et al.* 2015a; Prosdocimi *et al.* 2015, 2017) have used a smartphone camera for geomorphological studies. These authors assessed the advantages of the use of a smartphone. Certainly, the lens of a smartphone camera is not comparable with other commercial cameras, but the main disadvantage of the smartphone camera is the need to purchase apps or accessories to improve the flexibility of the conditions of image acquisition. Furthermore, smartphone camera lenses are non-measuring lenses, i.e., lenses that are not designed for surveying aims. For this reason, smartphone camera lenses have greater lens distortion compared to metric cameras. Therefore, it is very important to apply a correction to the lens distortion through calibration of the camera.

In addition, smartphone cameras have an autofocus function. The autofocus application modifies the focus distance by maximizing the sharpness of some reference points in the frames' images. Thus, for a good performance of the surface reconstruction, it is important to disable the autofocus before the image acquisition.

In this paper, videos were filmed instead of taking photographs, and the frames extracted from the videos were used. Over 2,800 frames were available to the plot reconstruction; and a high number of images can counteract the possible disadvantages of the SfM method (Eltner *et al.* 2015). Also, Micheletti *et al.* (2015a) stressed that the number of images in an SfM application is absolutely critical. In fact, increasing the number of frames may produce denser meshes and can improve model accuracy.

The use of a smartphone camera for SfM reconstruction requires an operation procedure for the image acquisition, described by Micheletti *et al.* (2015b), and an accurate analysis of the errors. In particular, as stressed by Micheletti *et al.* (2015a), registration uncertainty due to the rotation, translation and scaling transformation has to be assessed. If two datasets are available, the ICP algorithm allows minimization of the transformation errors and the differences between SfM and TLS datasets can be interpreted as approach-dependent errors (Micheletti *et al.* 2015a). In this paper the ICP procedure was used.

The GCPs coordinates collected by a total station were used to evaluate the georeferencing errors. The georeferencing errors (RMSE) obtained for each SfM point cloud were comparable to findings in similar studies (Micheletti *et al.* 2015a; Prosdocimi *et al.* 2015).

In this paper, a homogeneous surface was detected with good results contrary to Micheletti *et al.* (2015a), who stressed that the features in this type of subject are very difficult to match by the automatic feature matching process. This probably happens because the performance of SfM photogrammetry is scale dependent and in this case study an experimental plot was surveyed.

However, the comparison between the TLS and SfM surveys showed slight differences. The TLS survey was used as reference, although the accuracy of the type of TLS used seems not to be ideal for the aim of this study. In fact, the accuracy of the TLS obtained using ten check points was high for the assessment of soil erosion. The maps obtained by the C2C and DEM comparisons between SfM and TLS showed, for the second survey, an anomalous area on the right side of the plot. This area, near the galvanized sheet, represents a depressional area, as illustrated by the frames obtained by the Apple iPhone 6 Plus. The results obtained from the evaluation of the soil loss using TLS showed an underestimation of the actual soil loss, so this lowest area could be the cause of the 26% area of TLS underestimation.

The results confirmed those obtained by Smith & Vericat (2015) at small scale and there is no reason to prefer the TLS survey to SfM.

CONCLUSIONS

The purpose of the paper was to evaluate the suitability of SfM photogrammetry methods, using a smartphone

camera, for event soil erosion assessment when interrill erosion occurs. To assess the capability of the camera, a TLS was used. For each method, two DEMs of the surface of a 2×11 m plot were determined before and after a rainfall event. A calibration of the Apple iPhone 6 Plus was made before the dense point cloud construction. The coordinates of control points derived from the SfM and TLS were first compared with the ones obtained from a total station. The georeferencing errors were obtained, about 0.005 m (mean value derived from the two surveys) for the SfM and 0.003 m (mean value derived from the two surveys) for the TLS. For the TLS, registration errors also have to be considered, about 0.006 m.

The SfM validation using a TLS dataset was done. The cloud-to-cloud comparison was made considering the TLS point cloud as reference. The results showed a good agreement for the second survey (MAE = 0.009 m, SDE = 0.008 m, and RMSE = 0.011 m), while for the first survey a greater difference was observed (MAE = 0.015 m, SDE = 0.01 m, and RMSE = 0.018 m). Analogous results were obtained by the difference of DEM (DoD, obtained by the subtraction of DEM_{new}-DEM_{old}) comparison although with lower error values (MAE = 0.012 m, SDE = 0.006 m, and RMSE = 0.015 m for the first survey; MAE = 0.001 m, SDE = 0.007 m, and RMSE = 0.005 m for the second survey). This slight difference could be due to the rasterization process. However, as shown below, the TLS underestimates the soil loss, so the differences observed for the first survey could be due to some problems with the TLS survey.

Before the evaluation of the soil surface variations induced by the erosive event, an analysis of the DoDs uncertainty was made. In particular, using an interval confidence of 90%, the method of Wheaton *et al.* (2010) was applied and the minimum level of detection ($_{min}$LoD) was determined.

The $_{min}$LoD was used to identify the real lowering/raising from the uncertainty areas on the DoDs. A smartphone camera appears appropriate and sensitive for detecting small soil surface variations induced by low erosive events.

Furthermore, an analysis of the changes in surface elevation subsequent to the erosive event was made. A negative value in the cells of the DoDs was interpreted as erosion (surface lowering), a positive value as deposition, and a very low or zero value as no change (Martínez-Casasnovas *et al.* 2002). The results showed that the TLS underestimated the soil loss by about 26% while the SfM seems to detect correctly the soil loss. This first result is important because for the application of the SfM Photogrammetry a smartphone camera was used. This is less expensive than TLS and more easily accessible.

ACKNOWLEDGEMENTS

This research was financially supported by C.R.P. cod. 2015.0350 021.

REFERENCES

Agassi, M. & Bradford, J. M. 1999 Methodologies for interrill soil erosion studies. *Soil & Tillage Research* **49**, 277–287.

Aucelli, P. P. C., Conforti, M., Della Seta, M., Del Monte, M., D'uva, L., Rosskopf, C. M. & Vergari, F. 2016 Multi-temporal digital photogrammetric analysis for quantitative assessment of soil erosion rates in the Landola catchment of the Upper Orcia Valley (Tuscany, Italy). *Land Degradation and Development* **27** (4), 1075–1092.

Brevik, E. C., Cerdà, A., Mataix-Solera, J., Pereg, L., Quinton, J. N., Six, J. & Van Oost, K. 2015 The interdisciplinary nature of SOIL. *Soil* **1**, 117–129. doi:10.5194/soil-1-117-2015.

Brown, D. C. 1966 Decentering distortion of lenses. *Photogrammetric Engineering* **32** (3), 444–462.

Cao, L., Zhang, K., Dai, H. & Liang, Y. 2015 Modeling interrill erosion on unpaved roads in the Loess Plateau of China. *Land Degradation and Development* **26** (8), 825–832. doi:10.1002/ldr.2253.

Castillo, C., Pérez, R., James, M. R., Quinton, J. N., Taguas, E. V. & Gómez, J. A. 2012 Comparing the accuracy of several field methods for measuring gully erosion. *Soil Science Society of America Journal* **76** (4), 1319–1332.

Cerdà, A., González-Pelayo, O., Giménez-Morera, A., Jordán, A., Pereira, P., Novara, A., Brevik, E. C., Prosdocimi, M., Mahmoodabadi, M., Keesstra, S., García Orenes, F. & Ritsema, C. 2016 The use of barley straw residues to avoid high erosion and runoff rates on persimmon plantations in Eastern Spain under low frequency–high magnitude simulated rainfall events. *Soil Research* **54**, 154–165. doi: 10.1071/SR15092.

Eltner, A. & Baumgart, P. 2015 Accuracy of terrestrial Lidar data for soil erosion measurement: application to a Mediterranean field plot. *Geomorphology* **245**, 243–254.

Eltner, A., Mulsow, C. & Maas, H.-G. 2013 Quantitative measurement of soil erosion from TLS and UAV data. *International Archives of the Photogrammetry, Remote Sensing and Spatial Information Sciences – ISPRS Archives* **40**, 119–124.

Eltner, A., Kaiser, A., Castillo, C., Rock, G., Neugirg, F. & Abellan, A. 2015 Image-based surface reconstruction in geomorphometry – merits, limits and developments of a promising tool for geoscientists. *Earth Surface Dynamics* **3**, 1445–1508. doi:10.5194/esurfd-3-1445-2015.

Eltner, A., Kaiser, A., Castillo, C., Rock, G., Neugirg, F. & Abellán, A. 2016 Image-based surface reconstruction in geomorphometry-merits, limits and developments. *Earth Surface Dynamics* **4** (2), 359–389.

FAO-ISRIC-ISSS 1998 *World Reference Base for Soil Resources*. World Soil Resources Report, **84**, FAO, Rome, Italy, p. 90.

Filin, S., Goldshleger, N., Abergel, S. & Arav, R. 2013 Robust erosion measurement in agricultural fields by colour image processing and image measurement. *European Journal of Soil Science* **64**, 80–91.

Frankl, A., Stal, C., Abraha, A., Nyssen, J., Rieke-Zapp, D., De Wulf, A. & Poesen, J. 2015 Detailed recording of gully morphology in 3D through image-based modeling. *Catena* **127**, 92–101.

Gómez, J. A. & Nearing, M. A. 2005 Runoff and sediment losses from rough and smooth soil surfaces in a laboratory experiment. *Catena* **59** (3), 253–266.

Helming, K., Römkens, M. J. M. & Prasad, S. N. 1998 Surface roughness related processes of runoff and soil loss: a flume study. *Soil Science Society of America Journal* **62** (1), 243–250.

Kaiser, A., Neugirg, F., Rock, G., Müller, C., Haas, F., Ries, J. & Schmidt, J. 2014 Small-scale surface reconstruction and volume calculation of soil erosion in complex Moroccan gully morphology using structure from motion. *Remote Sensing* **6** (8), 7050–7080.

Keesstra, S. D., Geissen, V., van Schaik, L., Mosse, K. & Piiranen, S. 2012 Soil as a filter for groundwater quality. *Current Opinions in Environmental Sustainability* **4**, 507–516. doi:10.1016/j.cosust.2012.10.007.

Keesstra, S. D., Bouma, J., Wallinga, J., Tittonell, P., Smith, P., Cerdà, A., Montanarella, L., Quinton, J. N., Pachepsky, Y., van der Putten, W. H., Bardgett, R. D., Moolenaar, S., Mol, G., Jansen, B. & Fresco, L. O. 2016 The significance of soils and soil science towards realization of the United Nations Sustainable Development Goals. *Soil* **2**, 111–128. doi:10.5194/soil-2-111-2016.

Martínez-Casasnovas, J. A. 2000 A spatial information technology approach for the mapping and quantification of gully erosion. In: *Int. Symp. on Gully Erosion under Global Change*, Book of Abstracts, K.U. Leuven, Leuven, p. 89.

Martínez-Casasnovas, J. A., Ramos, M. C. & Ribes-Dasi, M. 2002 Soil erosion caused by extreme rainfall events: mapping and quantification in agricultural plots from very detailed digital elevation models. *Geoderma* **105** (1–2), 125–140. doi:10.1016/S0016-7061(01)00096-9.

Martín-Moreno, C., Martín Duque, J. F., Nicolau Ibarra, J. M., Hernando Rodríguez, N., Sanz Santos, M. A. & Sánchez Castillo, L. 2016 Effects of topography and surface soil cover on erosion for mining reclamation: the experimental spoil heap at El Machorro Mine (Central Spain). *Land Degradation and Development* **27** (2), 145–159. doi:10.1002/ldr.2232.

Micheletti, N., Chandler, J. H. & Lane, S. N. 2015a Investigating the geomorphological potential of freely available and accessible structure-from-motion photogrammetry using a smartphone. *Earth Surfaxe Processes and Landforms* **40** (4), 473–486.

Micheletti, N., Chandler, J. H. & Lane, S. N. 2015b Structure from Motion (SFM) photogrammetry. In: *Geomorphological Techniques* (L. E. Clarke & J. M. Nield, eds). British Society for Geomorphology, London, UK.

Navarro-Hevia, J., Lima-Farias, T. R., de Araújo, J. C., Osorio-Peláez, C. & Pando, V. 2016 Soil erosion in steep road cut slopes in Palencia (Spain). *Land Degradation and Development* **27** (2), 190–199. doi:10.1002/ldr.2459.

Nouwakpo, S. K. & Huang, C. 2012 A simplified close-range photogrammetric technique for soil erosion assessment. *Soil Science Society of America Journal* **76** (1), 70–84.

Nouwakpo, S. K., James, M. R., Weltz, M. A., Huang, C.-H., Chagas, I. & Lima, L. 2014 Evaluation of structure from motion for soil micro topography measurement. *The Photogrammetric Record* **29**, 297–316. doi:10.1111/phor.12072.

Ochoa, P. A., Fries, A., Mejía, D., Burneo, J. I., Ruíz-Sinoga, J. D. & Cerdà, A. 2016 Effects of climate, land cover and topography on soil erosion risk in a semiarid basin of the Andes. *Catena* **140**, 31–42. doi:10.1016/j.catena.2016.01.011.

Ouédraogo, M. M., Degré, A., Debouche, C. & Lisein, J. 2014 The evaluation of unmanned aerial system-based photogrammetry and terrestrial laser scanning to generate DEMs of agricultural watersheds. *Geomorphology* **214**, 339–355.

Pérez-Cabello, F., Cerdà, A., De La Riva, J., Echeverría, M. T., García-Martín, A., Ibarra, P., Lasanta, T., Montorio, R. & Palacios, V. 2012 Micro-scale post-fire surface cover changes monitored using high spatial resolution photography in a semiarid environment: a useful tool in the study of post-fire soil erosion processes. *Journal of Arid Environments* **76** (1), 88–96. doi:10.1016/j.jaridenv.2011.08.007.

Prosdocimi, M., Calligaro, S., Sofia, G., Dalla Fontana, G. & Tarolli, P. 2015 Bank erosion in agricultural drainage networks: new challenges from structure-from-motion photogrammetry for post-event analysis. *Earth Surface Processes and Landforms* **40**, 1891–1906.

Prosdocimi, M., Burguet, M., Di Prima, S., Sofia, G., Terol, E., Comino, J. R., Cerdà, A. & Tarolli, P. 2017 Rainfall simulation and Structure-from-Motion photogrammetry for the analysis of soil water erosion in Mediterranean vineyards. *Science of the Total Environment* **574**, 204–215.

Rodrigo Comino, J., Iserloh, T., Lassu, T., Cerdà, A., Keesstra, S. D., Prosdocimi, M., Brings, C., Marzen, M., Ramos, M. C., Senciales, J. M., Ruiz Sinoga, J. D., Seeger, M. & Ries, J. B. 2016 Quantitative comparison of initial soil erosion processes and runoff generation in Spanish and German vineyards. *Science of the Total Environment* **565**, 1165–1174.

Smith, M. W. & Vericat, D. 2015 From experimental plots to experimental landscapes: topography, erosion and deposition in sub-humid badlands from Structure-from-Motion

photogrammetry. *Earth Surface Processes and Landforms* **40** (12), 1656–1671.

Smith, M. W., Carrivick, J. L. & Quincey, D. J. 2015 Structure from motion photogrammetry in physical geography. *Progress in Physical Geography* **40** (2), 247–275.

Snapir, B., Hobbs, S. & Waine, T. W. 2014 Roughness measurements over an agricultural soil surface with Structure from Motion. *ISPRS Journal of Photogrammetry and Remote Sensing* **96**, 210–223.

Tarolli, P., Sofia, G., Calligaro, S., Prosdocimi, M., Preti, F. & Dalla Fontana, G. 2015 Vineyards in terraced landscapes: new opportunities from Lidar data. *Land Degradation and Development* **26** (1), 92–102. doi:10.1002/ldr.2311.

Thompson, S. E., Katul, G. G. & Porporato, A. 2010 Role of micro topography in rainfall-runoff partitioning: an analysis using idealized geometry. *Water Resources Research* **46** (7). doi: 10.1029/2009WR008835.

Todisco, F., Vergni, L., Mannocchi, F. & Bomba, C. 2012 Calibration of the soil loss measurement method at the Masse experimental station. *Catena* **91**, 4–9.

Ullman, S. 1979 The interpretation of structure from motion. *Proceedings of the Royal Society B* **203**, 405–426.

Vericat, D., Smith, M. W. & Brasington, J. 2014 Patterns of topographic change in sub-humid badlands determined by high resolution multi-temporal topographic surveys. *Catena* **120**, 164–176.

Vinci, A., Brigante, R., Todisco, F., Mannocchi, F. & Radicioni, F. 2015 Measuring rill erosion by laser scanning. *Catena* **124**, 97–108. doi: http://dx.doi.org/10.1016/j.catena.2014.09.003.

Vinci, A., Todisco, F. & Mannocchi, F. 2016 Calibration of manual measurements of rills using terrestrial laser scanning. *Catena* **140**, 164–168. doi: 10.1016/j.catena.2016.01.026.

Wheaton, J. M., Brasington, J., Darby, S. E. & Sear, D. A. 2010 Accounting for uncertainty in DEMs from repeat topographic surveys: improved sediment budgets. *Earth Surface Processes and Landforms* **35** (2), 136–156.

Zhao, X., Wu, P., Gao, X. & Persaud, N. 2015 Soil quality indicators in relation to land use and topography in a small catchment on the Loess Plateau of China. *Land Degradation and Development* **26** (1), 54–61. doi:10.1002/ldr.2199.

First received 1 March 2016; accepted in revised form 16 January 2017. Available online 2 March 2017